# Canted antiferromagnetic order in the centrosymmetric honeycomb-lattice compound NdP $t_6$ $Al_3$

R. Oishi, C. Ritter, M. M. Koza, D. T. Adroja, T. Onimaru, Y. Shimura, K. Umeo, and T. Takabatake

**Published version information**

**Citation:** R. Oishi (et.al) Canted antiferromagnetic order in the centrosymmetric honeycomb-lattice compound NdP $t_6$ $Al_3$, Phys. Rev. B **110**, 144411

**DOI:** https://doi.org/10.1103/PhysRevB.110.144411

# Canted antiferromagnetic order in the centrosymmetric honeycomb-lattice compound $NdPt_6Al_3$

R. Oishi,[1,*] C. Ritter,[2] M. M. Koza,[2] D. T. Adroja,[3,4] T. Onimaru,[1] Y. Shimura,[1] K. Umeo,[5] and T. Takabatake[1]

[1]*Department of Quantum Matter, Graduate School of Advanced Science and Engineering, Hiroshima University, Higashi-Hiroshima 739–8530, Japan*

[2]*Institut Laue Langevin, Boîte Postale 156, 38042 Grenoble Cedex 9, France*

[3]*ISIS Facility, STFC, Rutherford Appleton Laboratory, Chilton, Didcot, Oxfordshire OX11 0QX, United Kingdom*

[4]*Highly Correlated Matter Research Group, Physics Department, University of Johannesburg, Auckland Park 2006, South Africa*

[5]*Department of Low Temperature Experiment, Integrated Experimental Support/Research Division, N-BARD, Hiroshima University, Higashi-Hiroshima 739–8526, Japan*

(Received 9 August 2024; accepted 23 September 2024; published 7 October 2024)

The magnetic properties of $NdPt_6Al_3$ with a honeycomb structure of Nd ions have been studied by magnetic susceptibility $M(T)/B$, isothermal magnetization $M(B)$, specific heat $C(T)$, and electrical resistivity $\rho(T)$ measurements using single-crystalline samples as well as by neutron diffraction and inelastic scattering using polycrystalline samples. A λ-type anomaly in $C(T)$, a bend in $\rho(T)$, and a jump in $M(T)/B_{\|a}$ occur concomitantly at 1.2 K, revealing a long-range magnetic order. A spontaneous moment of 0.2 $\mu_B$/f.u. (formula units) in the $M(B \parallel a)$ curve at 0.3 K suggests a canted antiferromagnetic (AFM) order with the $Nd^{3+}$ moments lying in the honeycomb plane. The inelastic neutron-scattering measurements disclose crystalline electric-field (CEF) excitations at 0.6 and 2.9 meV. The energy of the CEF excitations measured at 1.5 and 100 K, temperature dependences of $B/M(T)$, and two Schottky anomalies in $C(T)$ are simultaneously analyzed using a trigonal CEF model for the $J = 9/2$ multiplet of the $Nd^{3+}$ ion. The CEF doublet ground state is described as $|\psi\rangle = -0.082|\pm\frac{7}{2}\rangle + 0.555|\mp\frac{5}{2}\rangle \pm 0.827|\pm\frac{1}{2}\rangle$. The neutron powder-diffraction experiment determines the canted AFM structure defined with a propagation vector $\mathbf{k} = [0, 0, 0]$ and ordered moments of 2.62 $\mu_B$ canting by an angle of 15° from antiparallel alignment in the honeycomb plane. We propose that the canting of AFM moments results from the Dzyaloshinskii-Moriya interaction between the nearest-neighbor $Nd^{3+}$ moments at the midpoint of which the inversion symmetry is broken by the presence of the Pt triangle inside the Nd hexagon.

DOI: 10.1103/PhysRevB.110.144411

## I. INTRODUCTION

Unconventional magnetic orders and novel quantum states in honeycomb-lattice compounds have attracted much interest in recent years [1–9]. Unlike in the triangular lattice or pyrochlore one, the nearest-neighbor (NN) antiferromagnetic (AFM) interaction in the honeycomb lattice does not give rise to geometrical frustration but leads to a Néel-type AFM order. If the NN AFM interaction in the honeycomb lattice competes with the next-nearest-neighbor (NNN) and/or next-next-nearest-neighbor ones, then a magnetic frustration occurs. Consequently, the Néel-type order becomes unstable, leading to zigzag, stripe, and noncollinear magnetic orders [1–7]. The strength of the magnetic frustration is characterized by a frustration parameter $f = |\theta_p|/T_m$, where $\theta_p$ is the paramagnetic Curie temperature and $T_m$ is the magnetic transition temperature [10]. The magnetic frustration can produce disordered states called plaquette valence-bond solid and columnar states [8,9]. Such frustrated magnetic states in honeycomb lattices have been explored mostly for insulators and semiconductors [11–13]. Furthermore, a Kitaev model for honeycomb magnets with bond-dependent anisotropic exchange interactions between the NN spins has a quantum spin liquid state as the ground state [14]. This theory stimulated experimental investigations of insulating honeycomb magnets based on 4*d* and 5*d* transition elements in search of quantum spin liquids [15].

In addition to the magnetic frustration, the lack of local inversion symmetry in the honeycomb lattice induces unconventional magnetic structures. At the site of magnetic-ion decorated honeycomb lattice, the local inversion symmetry breaks. This condition is a key for stabilizing odd-parity magnetic toroidal multipoles such as a vortexlike magnetic structure and a *z*-type AFM structure [16,17]. The local inversion symmetry breaks also at the midpoint of NNN bond in the honeycomb lattice. The lack of inversion symmetry is a requisite to activate a Dzyaloshinskii-Moriya (DM) interaction between the magnetic ions, which tends to orient the magnetic moments $\mathbf{m}_i$ and $\mathbf{m}_j$ perpendicular to each other [18]. The DM interaction term is expressed by $\mathbf{D}$ $(\mathbf{m}_i \times \mathbf{m}_j)$, where the direction of $\mathbf{D}$ is determined by Moriya's rules [19]. Moreover, a magnon Hall effect has been predicted to be induced by the DM interaction in the honeycomb lattice [20,21].

In the insulating magnets, direct exchange- and superexchange interactions are usually dominant. In the rare-earth based intermetallic compounds, on the other hand, Ruderman-Kittel-Kasuya-Yosida (RKKY) exchange interactions

*Contact author: oishi@hiroshima-u.ac.jp

 

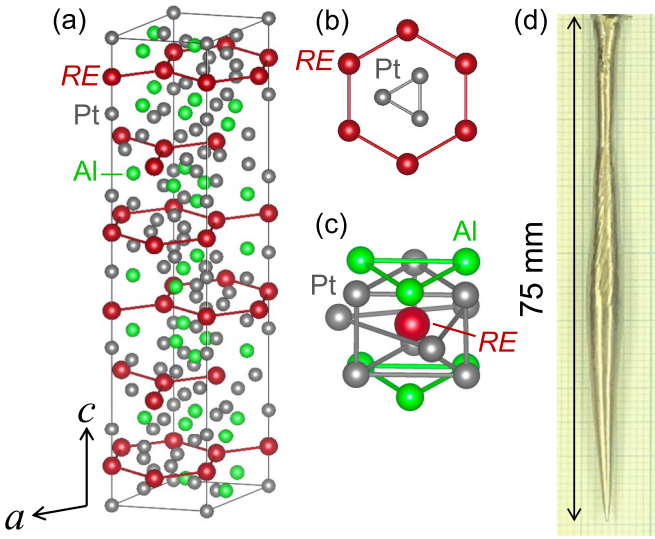


FIG. 1. (a) Trigonal crystal structure of $RE\mathrm{Pt_6Al_3}$ with the space group of $R\bar{3}c$. (b) Hexagon of rare-earth ions centered by a triangle of Pt atoms. (c) Local structure around the rare-earth ion. (d) Photograph of the single-crystalline sample of $\mathrm{NdPt_6Al_3}$ grown by the Czochralski method.

mediated by the conduction electrons are longer ranged than direct exchange and superexchange ones. The long-range RKKY interaction and magnetic frustration cooperate to make complex magnetic structures [22–24]. Among a large number of intermetallic honeycomb magnets based on rare-earth (*RE*) ions [25–31], only two series of compounds have a perfect honeycomb lattice with threefold rotational symmetry, to the best of our knowledge [29–31]. The first series is $RE\mathrm{Ni_3}X_9$ ($RE$ = Gd–Yb; $X$ = Al and Ga) crystallizing in the $\mathrm{ErNi_3Al_9}$-type trigonal structure with the noncentrosymmetric point group $R32$ [29,30]. The absence of the space inversion symmetry in this structure originates a DM interaction whose $D$ vector is along the $c$ axis. If the magnetic moments lie in the honeycomb plane, the DM interaction cants the parallel or antiparallel moments, stabilizing a canted AFM structure or a helical magnetic structure [32–34]. The direction of the magnetic moments in this series has been explained by considering the crystalline electric field (CEF) effects and the RKKY interaction among NN and NNN *RE* moments in the honeycomb plane [35].

The second series is $RE\mathrm{Pt_6Al_3}$ ($RE$ = Ce, Pr, Nd, Sm, Gd, and Tb) crystallizing in the $\mathrm{NdPt_6Al_3}$-type trigonal structure with the centrosymmetric space-group $R\bar{3}c$ [31]. The *RE* atoms (Wyckoff site 12$c$) are arranged on the honeycomb structure centered by a Pt triangle as shown in Fig. 1(b). In the unit cell shown in Fig. 1(a), six $RE_2\mathrm{Pt_3}$ layers are stacked along the $c$ axis. The *RE* ion is sandwiched between Pt and Al triangles, preserving a $C_3$ symmetry for the *RE* ion [see Fig. 1(c)].

Among the $RE\mathrm{Pt_6Al_3}$ series, $\mathrm{GdPt_6Al_3}$ orders below 7.4 K into a canted AFM structure with a spontaneous moment of 0.1 $\mu_B$/f.u. (formula units) in the honeycomb plane [36]. The canting of the magnetic moments for $\mathrm{GdPt_6Al_3}$ was ascribed to the DM interaction between the NN Gd ions with the D vector pointing along the $c$ axis. Since the Pt triangle centers at the *RE* hexagon shown in Fig. 1(b), the midpoint of NN *RE* ions lacks inversion symmetry. Therefore, the DM interaction may cant the Gd moments even in the compound with the centrosymmetric space group $R\bar{3}c$. On the other hand, $\mathrm{SmPt_6Al_3}$ orders below 6.5 K into a collinear AFM structure with the moments pointing toward the $c$ axis [37]. However, the large absorption cross sections of Sm and Gd nuclei for thermal neutrons make it difficult to determine the magnetic structures of $RE\mathrm{Pt_6Al_3}$ with $RE$ = Sm and Gd by means of the neutron-diffraction technique.

In order to gain insight into the relation between CEF-level scheme and magnetic structures for the $RE\mathrm{Pt_6Al_3}$ series, we selected $\mathrm{NdPt_6Al_3}$ in which the $\mathrm{Nd^{3+}}$ ion with $4f^3$ electrons has a total angular moment of $J = 9/2$. In a previous study with a polycrystalline sample of $\mathrm{NdPt_6Al_3}$, no magnetic order was observed down to 3 K by magnetic susceptibility measurements [31]. In this paper, we report the magnetic and transport properties of single-crystalline samples of $\mathrm{NdPt_6Al_3}$, revealing an AFM transition at 1.2 K. The combined analysis of the specific-heat and magnetic susceptibility data of single crystals, and the neutron-diffraction and inelastic-scattering data of polycrystals allowed us to determine the magnetic structure and the CEF-level scheme of $\mathrm{NdPt_6Al_3}$.

## II. EXPERIMENTS

A single-crystalline sample of $\mathrm{NdPt_6Al_3}$ was grown by the Czochralski method from a stochiometric melt of 15 g in a tungsten crucible heated in an rf induction furnace. A 75-mm-long crystal rod was obtained by pulling a seed rod at a speed of 8 mm/h. A photo of the crystal rod is shown in Fig. 1(d). The atomic compositions of several parts were examined by wavelength-dispersive electron-probe microanalysis (EPMA). The EPMA showed that the whole crystal has the stoichiometric composition of $\mathrm{NdPt_6Al_3}$ within 1% resolution. As an impurity, a small amount of $\mathrm{Pt_5Al_3}$ was detected. The crushed sample was used for powder x-ray-diffraction measurement with Cu K$\alpha$ radiation. A Rietveld analysis of the diffraction data yielded trigonal lattice parameters as $a = 7.5471(2)$ Å and $c = 39.252(1)$ Å, values which are in good agreement with the reported ones [31].

The single crystal was oriented by the backreflection Laue x-ray pattern for the measurements of magnetization $M(T, B)$, electrical resistivity $\rho(T)$, and specific heat $C(T)$. The oriented crystal was cut into appropriate dimensions for each measurement by spark erosion. We used a Quantum Design MPMS SQUID (superconducting quantum interference device) magnetometer for the measurements of $M(T, B)$ from 1.8 to 300 K in magnetic fields $B$ up to 5 T. In a range from 0.3 to 2 K, $M(T, B)$ was measured up to $B = 8.5$ T by a laboratory-built capacitively detected Faraday magnetometer in a $^3$He cryostat. A four-terminal ac method was used for $\rho(T)$ measurements from 0.05 to 3 K in various constant magnetic fields up to 6 T with an adiabatic demagnetization refrigerator mF-ADR50. For $\rho(T)$ measurements in zero field from 3 to 300 K, a Gifford–McMahon-type refrigerator was used. The field dependence of $\rho(B)$ was measured in the longitudinal configuration $B \parallel I$ up to 6 T at constant temperatures down to 0.3 K with the mF-ADR50. The measurement of $C(T)$ from 0.4 to 100 K was performed in constant external fields up to

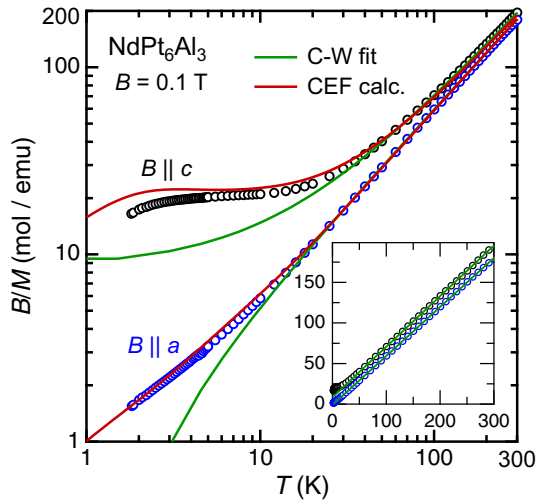


FIG. 2. Temperature dependence of the inverse magnetic susceptibility $B/M(T)$ of $NdPt_6Al_3$ single crystal for the magnetic fields $B \parallel a$ and $B \parallel c$. The fits to the data for $T > 100$ K with a Curie-Weiss form are shown by the solid lines (green). The solid lines (red) represent the calculated $B/M(T)$ data by using the CEF model for the $Nd^{3+}$ ion (see text).

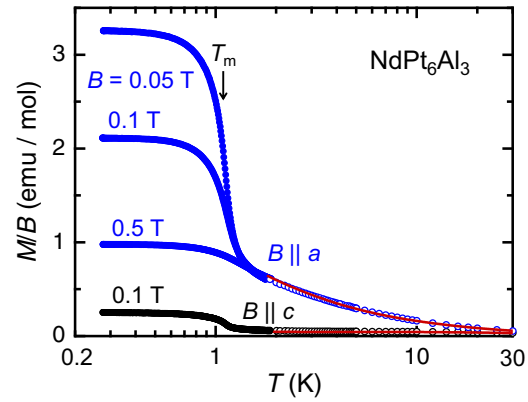


FIG. 3. Temperature dependence of $M(T)/B$ of $NdPt_6Al_3$ single crystal in different constant magnetic fields for $B \parallel a$ and $B \parallel c$. The solid lines (red) for $T > 2$ K represent the calculated data by using the CEF model for the $Nd^{3+}$ ion (see text).

9 T by the relaxation method with a Quantum Design Physical Property Measurement System (PPMS).

For neutron-scattering and -diffraction experiments, we prepared polycrystalline samples of $NdPt_6Al_3$ by arc melting stoichiometric quantities of the elements with subsequent annealing at 1100 °C for 10 days. As a reference to evaluate the phonon contribution, we prepared polycrystalline samples of $YPt_6Al_3$ by a similar method as for $NdPt_6Al_3$. The inelastic neutron-scattering (INS) spectra were collected by using the thermal neutron time-of-flight spectrometer PANTHER at the Institute Laue-Langevin (ILL), Grenoble, France [38]. The powdered sample of 10 g was wrapped by Al foil and mounted inside a cylindrical Al can. Measurements were performed at 1.8 and 100 K with incident energies $E_i$ between 8.75 and 35 meV [39]. The collected data have been analyzed using the software MANTID to obtain the CEF-level scheme [40].

To determine the magnetic structure, neutron powder-diffraction experiments were performed with the high-intensity D1B powder diffractometers at ILL. The powdered sample of 10 g was introduced in the cylindrical Cu sample holder (5-mm diameter) with He-exchange gas, which was set in a $^3He - {}^4He$ dilution cryostat. The diffraction measurements were carried out in zero field between 0.05 and 1.6 K [41]. Rietveld refinements were done using the software FULLPROF [42].

## III. RESULTS AND DISCUSSION

### A. Magnetic susceptibility and magnetization

The temperature dependence of the inverse magnetic susceptibility $B/M(T)$ of $NdPt_6Al_3$ in $B = 0.1$ T is shown in the inset of Fig. 2. The data at $T > 100$ K for both $B \parallel a$ and $B \parallel c$ follow a Curie-Weiss (CW) form, $M(T)/B = N_A\mu_{eff}^2/3k_B(T - \theta_p)$, where $N_A$ is the Avogadro number, $\mu_{eff}$ the effective magnetic moment, and $k_B$ the Boltzmann constant. The obtained values of $\mu_{eff} = 3.6\,\mu_B$/f.u. for both $B \parallel a$ and $B \parallel c$ agree with 3.62 $\mu_B$, which is expected for a free $Nd^{3+}$ ion. The values of $\theta_p$ for $B \parallel a$ and $B \parallel c$ are 1.43 and −13.7 K, respectively, yielding the averaged $\theta_p$, $\theta_{ave} = (\theta_{||c} + 2\theta_{||a})/3$ of −3.6 K. The negative sign of $\theta_{ave}$ indicates the dominance of the AFM interactions.

The data of $B/M(T)$ are replotted in a double-logarithmic scale in Fig. 2. On cooling below 30 K, $B/M(T)$ deviates from the CW behavior, and the $B/M(T)$ data for $B \parallel c$ become several times larger than those for $B \parallel a$. The magnetic anisotropy manifests itself in the plots of $M(T)/B$ vs $T$ as shown in Fig. 3. The ratio $M_{||a}/M_{||c}$ at $B = 0.1$ T increases from 1.6 to 10.5 with decreasing temperature from 30 to 1.5 K. The anisotropic variations of $M(T)/B$ in the paramagnetic state are reproduced by the CEF model for the $Nd^{3+}$ ion in $NdPt_6Al_3$ as described below. The $M(T)/B_{||a}$ data largely increase on cooling below 1.5 K and gradually saturate below 1 K, indicating a magnetic ordering of $Nd^{3+}$ moments. The saturation value of $M(T)/B_{||a}$ decreases with increasing $B \parallel a$, behavior which mimics that of a ferromagnetic transition. Taking the midpoint of the jump in $M(T)/B_{||a}$ as a transition temperature $T_m$, the frustration parameter $f = |\theta_{ave}|/T_m$ is obtained as 3.6 K/1.2 K = 3. Because this value is much smaller than the values reported for highly frustrated Nd-honeycomb compounds, e.g., $f = 16.2$ for $CuNd_2Ge_2O_8$ [43], the magnetic frustration in $NdPt_6Al_3$ may not be so significant.

In the magnetically ordered state at 0.3 K, the isothermal magnetization $M(B)$ was measured up to 8.5 T. As shown in the inset of Fig. 4, $M(B \parallel a)$ has a spontaneous moment of 0.2 $\mu_B$/f.u., while $M(B \parallel c)$ has no spontaneous moment. With increasing $B$ up to 8.5 T, $M(B \parallel a)$ reaches 2.8 $\mu_B$/f.u., the value of which is smaller than 3.27 $\mu_B$/f.u., expected for a free $Nd^{3+}$ ion. Compared to these values, the spontaneous moment of 0.2 $\mu_B$/f.u. in $M(B \parallel a)$ is one order of magnitude smaller. Note that the magnitude of $M(B \parallel a)$ at 8.5 T is three times larger than that of $M(B \parallel c)$. This strong anisotropy in $M(B)$ indicates that the $Nd^{3+}$ magnetic moments in the ordered state are lying in the honeycomb plane. If all free $Nd^{3+}$ magnetic moments were oriented to one direction as in a simple ferromagnetic state, then a spontaneous moment of ∼3 $\mu_B$/f.u. would appear.

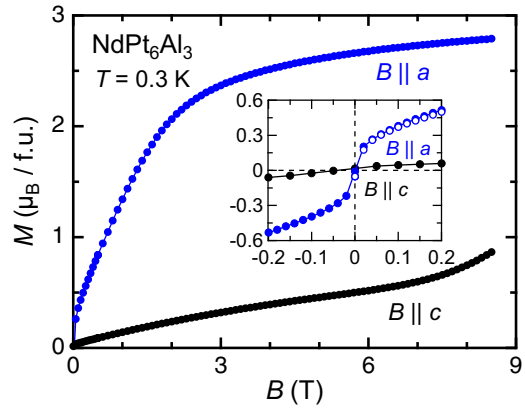


FIG. 4. Isothermal magnetization $M(B)$ curves of $NdPt_6Al_3$ at 0.3 K for $B \parallel a$ and $B \parallel c$. The inset shows the $M(B)$ data for $-0.2 \leqslant B \leqslant 0.2$ T. For $B \parallel a$, the open and closed circles, respectively, show the data collected upon increasing and decreasing magnetic fields.

Because this is not the case, the small spontaneous moment is probably a canted component of AFM moments in the honeycomb plane of $NdPt_6Al_3$ as found in a canted AFM state of $GdPt_6Al_3$ [36].

### B. Electrical resistivity

The temperature dependence of $\rho(T)$ of $NdPt_6Al_3$ from 300 to 0.05 K for the current directions $I \parallel a$ and $I \parallel c$ is shown in Fig. 5. The values of $\rho(300\ \text{K})$ for $I \parallel a$ and $I \parallel c$ are 36 and 100 μΩ cm, respectively. Upon cooling, both data of $\rho(T)$ monotonically decrease, keeping the relation $\rho(I \parallel c) \cong 2.8\ \rho(I \parallel a)$ in the whole temperature range. This contrasts with the very weak anisotropy in $\rho(T)$ for isostructural compounds $CePt_6Al_3$ and $GdPt_6Al_3$ [36,44]. We therefore attribute the anisotropic resistivity for $NdPt_6Al_3$ to possible stacking disorder of honeycomb layers along the $c$ axis [45,46].

The $\rho(T)$ data below 2 K in zero and various constant fields are shown in Figs. 6(a) and 6(b) for $I \parallel B \parallel a$ and $I \parallel B \parallel c$, respectively. In the zero field, both $\rho(T)$ curves bend at $T_m = 1.2$ K and decrease on cooling to 0.05 K. This value of $T_m$ agrees with the temperature at the midpoint of the increase in

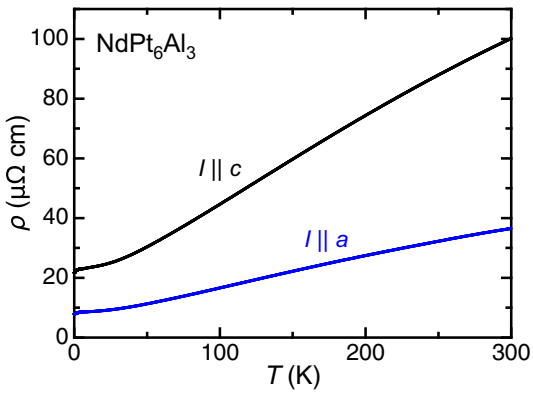


FIG. 5. Temperature dependences of the electrical resistivity $\rho(T)$ of $NdPt_6Al_3$ single crystal for the current directions $I \parallel a$ and $I \parallel c$.

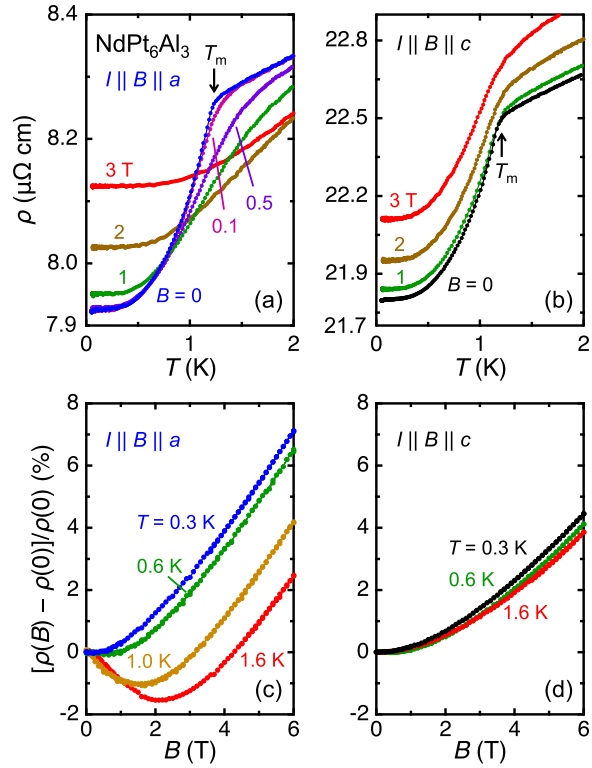


FIG. 6. Low-temperature electrical resistivity $\rho(T)$ of $NdPt_6Al_3$ single crystal in various magnetic fields of (a) $B \parallel a$ and (b) $B \parallel c$. Field dependence of normalized magnetoresistance, $\text{MR} = [\rho(B) - \rho(0)]/\rho(0)$, at different temperatures in longitudinal configurations (c) $I \parallel B \parallel a$ and (d) $I \parallel B \parallel c$.

$M(T)/B$ in $B \parallel a = 0.05$ T as shown in Fig. 3. The sharp bend at $T_m$ in zero field is blurred once an external field of 0.1 T is applied along the $a$ axis. With further increasing in $B \parallel a$, the bend in $\rho(T)$ is gradually smoothed with an increase in $T_m$. This dependence of $T_m$ on $B \parallel a$ is consistent with that of $M(T)/B_{||a}$ as shown in Fig. 3. On the contrary, application of $B \parallel c$ up to 2 T does not affect $T_m$ but increases the value of $\rho(T)$ for $T < 2$ K.

The field dependence of the electrical resistivity $\rho(B)$ was measured up to 6 T at several constant temperatures from 0.3 and 1.6 K. In Figs. 6(c) and 6(d), the $\rho(B)$ data are normalized as magnetoresistance (MR) $= [\rho(B) - \rho(0)]/\rho(0)$ for $I \parallel B \parallel a$ and $I \parallel B \parallel c$, respectively. For $I \parallel B \parallel a$, MR is positive at 0.3 and 0.6 K, while MR at 1.0 K $\leqslant T_m$ and 1.6 K $> T_m$ changes sign from negative to positive with increasing $B \parallel a$. The negative MR means the decrease in the scattering of conduction electrons by the Nd magnetic moments. Therefore, the sign change in MR suggests a change in the magnetic scattering mechanism. For $I \parallel B \parallel c$, on the other hand, the simply positive MR shows similar field dependence for both below and above $T_m$.

### C. Specific heat

The magnetic order in $NdPt_6Al_3$ at $T_m = 1.2$ K was observed in the specific heat $C(T)$. The inset of Fig. 7(a) shows the temperature dependence of the magnetic part of specific heat, $C_m(T)$, which was calculated by subtracting the $C(T)$ data

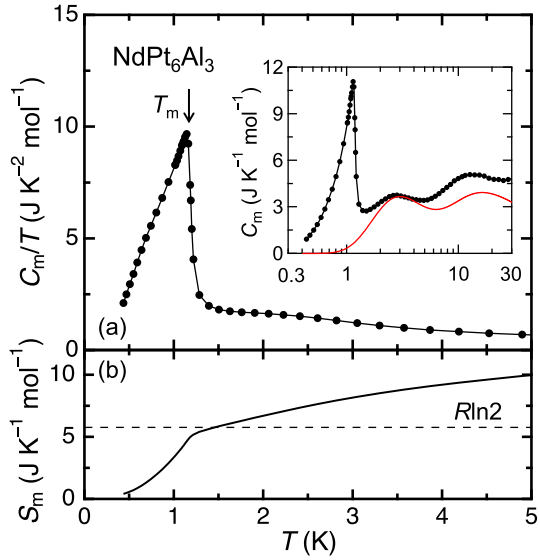


FIG. 7. Temperature dependences of (a) the magnetic specific heat $C_m$ divided by temperature, $C_m/T$, and (b) magnetic entropy $S_m(T)$ of $NdPt_6Al_3$. The inset shows the $C_m$ vs $T$ data. The solid line (red) is calculated by the CEF model for the $Nd^{3+}$ ion (see text).

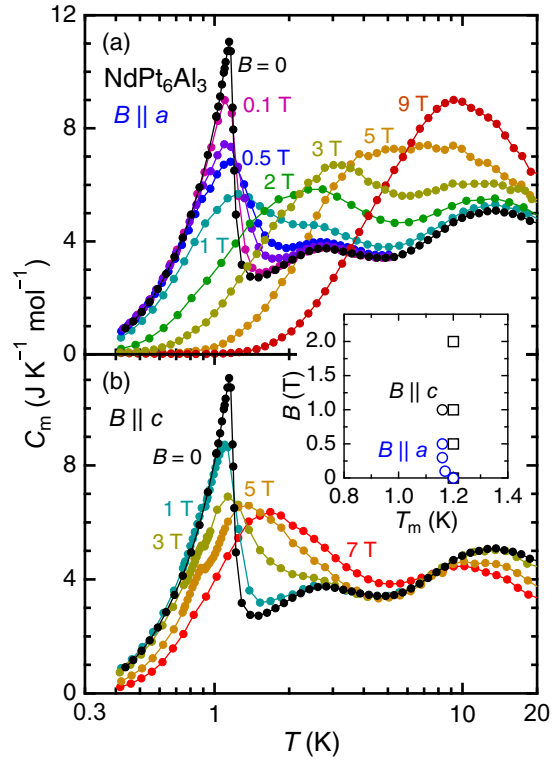


FIG. 8. Temperature dependence of $C_m$ of $NdPt_6Al_3$ at various constant magnetic fields applied for (a) $B \parallel a$ and (b) $B \parallel c$. The inset presents the magnetic field vs temperature phase diagram constructed from the data of $\rho(T)$ (squares) and $C_m(T)$ (circles) measured in constant magnetic fields.

for a nonmagnetic reference compound $YPt_6Al_3$ [44] from that for $NdPt_6Al_3$. In addition to a λ-type anomaly at $T_m = 1.2$ K due to the magnetic order, $C_m$ displays two rounded maxima at around 3 and 14 K. These maxima are explained as Schottky-type anomalies due to the thermal depopulation of the CEF levels, as will be shown later. The $C_m/T$ data are plotted vs $T$ in Fig. 7(a). We estimated the magnetic entropy $S_m(T)$ by integrating $C_m/T$ with respect to $T$. For $0 \leqslant T < 0.4$ K, we assumed that $C_m/T$ is described as $\gamma + \delta T^2 \exp(-\Delta/k_B T)$, where $\gamma = 5.5$ mJ/(K$^2$ mol) and $\Delta$ an anisotropic spin-wave gap [47]. As shown in Fig. 7(b), $S_m(T)$ reaches $0.89R\ln 2$ at $T_m = 1.2$ K, where $R$ is gas constant, indicating that the CEF ground state of the $Nd^{3+}$ ion is a doublet.

Figures 8(a) and 8(b) show the temperature dependences of $C_m$ in applied magnetic fields $B \parallel a$ and $B \parallel c$, respectively. The application of $B \parallel a$ to 0.5 T does not change the peak temperature but decreases the magnitude of the jump to half of that in $B = 0$. The λ-type anomaly disappears at $B \parallel a = 1$ T, and eventually at $B \parallel a = 9$ T, two Schottky peaks merge into a rounded maximum at around 10 K. For $B \parallel c$ up to 1 T, the λ-type anomaly remains at 1.2 K, but merges with the lower Schottky peak when $B \parallel c$ is increased to 5 T. The data of $\rho(T)$ and $C(T)$ measured in different constant magnetic fields are used to construct the partial $B$-$T$ phase diagram which is shown in the inset of Fig. 8. For $B \parallel a$, $T_m$ is not well defined above 0.5 T, whereas $T_m$ remains at 1.2 K for $B \parallel c$ up to 2 T. The weaker response of the bend in $\rho(T)$ and the λ-type anomaly in $C(T)$ to $B \parallel c$ compared to $B \parallel a$ is consistent with the fact that the magnetic hard direction is the $c$ axis as indicated by the isothermal magnetization.

### D. CEF-level scheme

The CEF excitations in $NdPt_6Al_3$ were investigated by INS experiments with two incident energies $E_i$ of 8.75 and 35 meV. Figures 9(a)–9(d) show color-coded plots of INS intensity as a function of energy-momentum transfers ($Q$) with $E_i = 8.75$ meV for $NdPt_6Al_3$ and $YPt_6Al_3$. In the $Q$-integrated (0 to 2 Å$^{-1}$) data at 1.5 K shown in Fig. 9(e), two clear magnetic excitations were observed at around 0.6 and 2.9 meV. Because these excitations are not present in $YPt_6Al_3$, they are CEF excitations between the $J = 9/2$ multiplets of the $Nd^{3+}$ ion. For the INS measurements with $E_i = 35$ meV, no extra magnetic excitations were observed in the energy range higher than 8.75 meV.

At 1.5 K, CEF transitions occur only from the doublet ground state to excited states as followed by the dipole selection rules. Therefore, the peaks at 0.6 meV (6.6 K) and 2.9 meV (34 K) are assigned to CEF excitations from the ground state to the first and second excited doublets, respectively. Note that this energy-level scheme is consistent with that derived from the $C_m(T)$ as shown with the (red) line in the inset of Fig. 7(a), where Schottky anomalies with two maxima at 3 and 14 K correspond to the excitation energies of 7.2 and 34 K, respectively. With increasing temperature to 100 K, an additional peak appears at around 2 meV in Fig 9(e), which seems to be the transition from the first excited CEF level at 0.6 meV to the second one at 2.9 meV. The magnetic scattering of the INS spectra was estimated by subtracting the scattering intensity of the nonmagnetic reference $YPt_6Al_3$ from that of $NdPt_6Al_3$. The spectra of magnetic scattering are represented in Fig. 9(f).

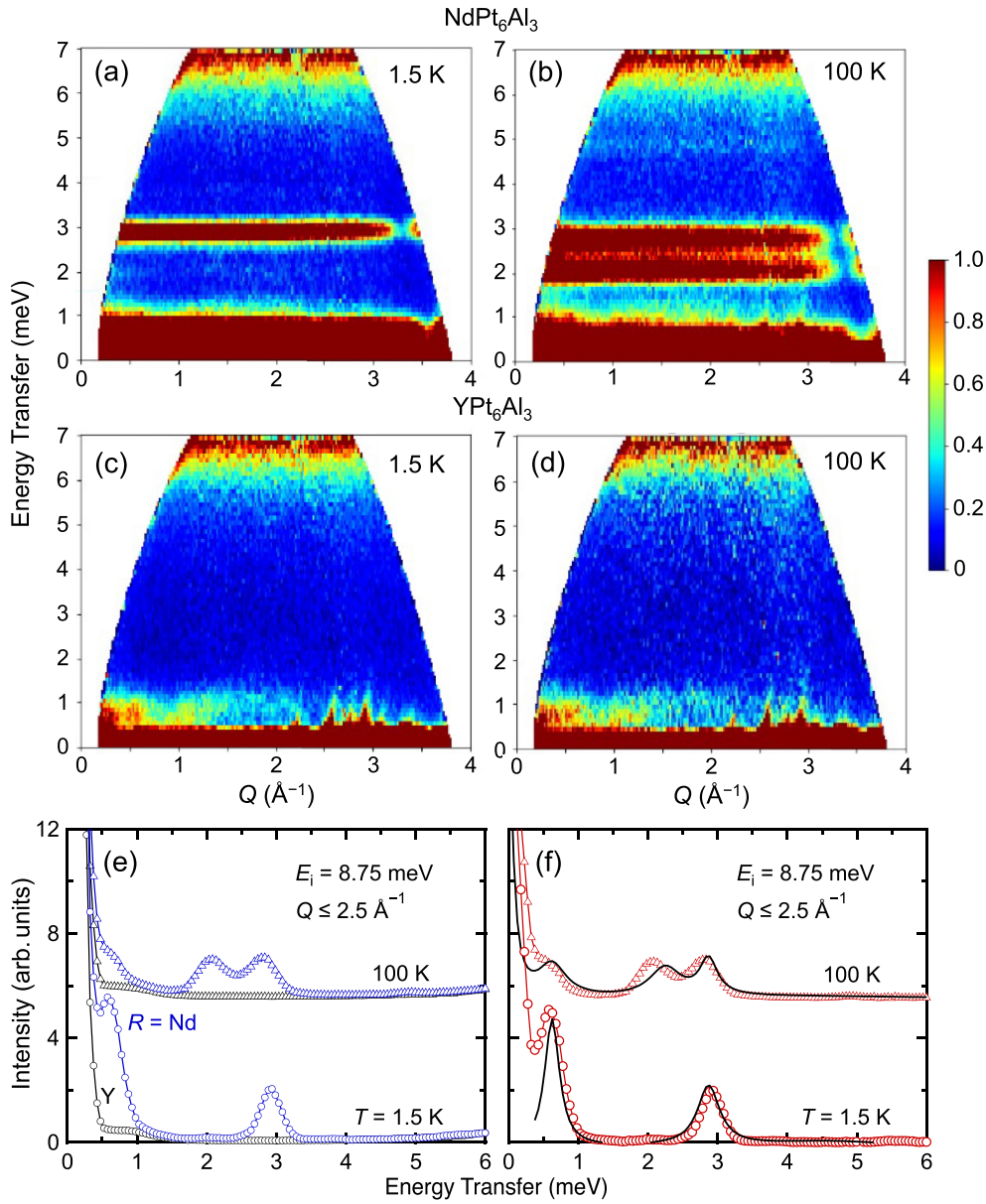


FIG. 9. Color-coded plots of the inelastic neutron-scattering intensity for $NdPt_6Al_3$ (a), (b) and $YPt_6Al_3$ (c), (d) as a function of energy transfer and momentum transfer with an incident energy $E_i = 8.75$ meV at 1.5 K (a), (c) and 100 K (b), (d). (e) Neutron-scattering intensity as a function of energy transfer obtained by integrating the data in a $|Q|$ range 0−2.5 Å$^{-1}$ for $NdPt_6Al_3$ (blue) and $YPt_6Al_3$ (black) at 1.5 and 100 K. The data at 100 K are offset for comparison. (f) The differential spectra (i.e., magnetic scattering) calculated by subtracting the intensity for $YPt_6Al_3$ from that for $NdPt_6Al_3$. The solid lines (black) show the fits based on the CEF model for the $Nd^{3+}$ ion.

The $J = 9/2$ multiplet of the $Nd^{3+}$ ion in a trigonal CEF is expected to split into five Kramers doublets. The point group of the $Nd^{3+}$ ion in $NdPt_6Al_3$ is trigonal $C_3$ as shown in Fig. 1(c). Taking the quantization axis as the trigonal $c$ axis, the CEF Hamiltonian, $\mathcal{H}_{\rm CEF}$, is described as below:

$$\mathcal{H}_{\rm CEF} = B_2^0 O_2^0 + B_4^0 O_4^0 + B_4^3 O_4^3 + B_6^0 O_6^0 + B_6^3 O_6^3 + B_6^6 O_6^6,$$

where $B_n^m$ are CEF parameters and $O_n^m$ the Stevens operator equivalents [48]. The CEF parameters were determined by the simultaneous fitting to the $B/M(T)$ and the INS data (at 1.5 and 100 K) using the CEF Hamiltonian. The parameters are obtained as $B_2^0 = 0.725$, $B_4^0 = -0.118 \times 10^{-1}$, $B_4^3 = 0.222$, $B_6^0 = -0.353 \times 10^{-3}$, $B_6^3 = -0.557 \times 10^{-2}$, and $B_6^6 = -0.539 \times 10^{-2}$ K, which give energy differences from the ground state to the four excited levels as 7.1, 33.2, 53.4, and 117.1 K. The CEF energy levels and the wave functions of the $Nd^{3+}$ ion in $NdPt_6Al_3$ are displayed in Fig. 10. Here, the wave function of the doublet ground state is given as $|\psi\rangle = -0.082|\pm\frac{7}{2}\rangle + 0.555|\mp\frac{5}{2}\rangle \pm 0.827|\pm\frac{1}{2}\rangle$ (double sign in same order). The fits to $B/M(T)$ data (for $B \parallel a$ and $B \parallel c$) and the INS data (at 1.5 and 100 K), respectively, are displayed in Figs. 2 and 9(f). The $C_{\rm m}(T)$ curve calculated with these parameters is drawn in the inset of Fig. 7(a). The curve moderately reproduces the two Schottky anomalies. Using the

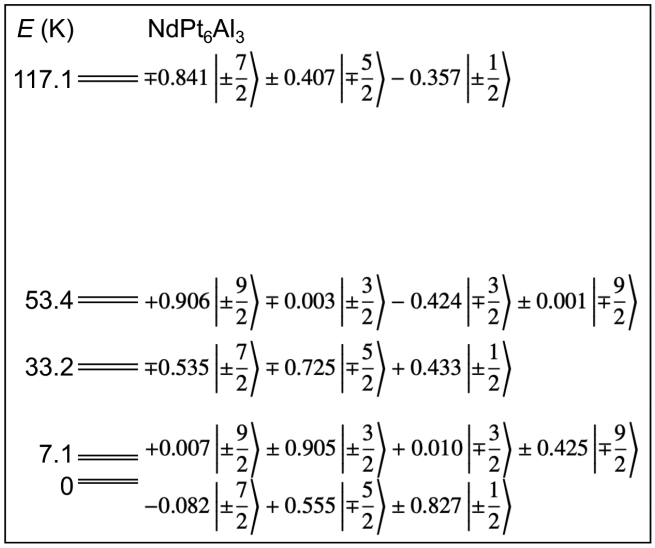


FIG. 10. CEF energy levels and the wave functions (double sign in same order) for the $Nd^{3+}$ ion in $NdPt_6Al_3$ calculated by the CEF parameters.

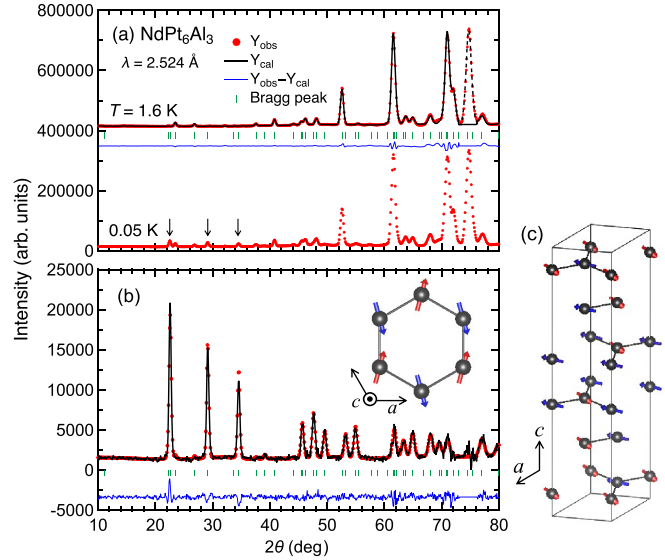


FIG. 11. (a) Neutron powder-diffraction patterns of $NdPt_6Al_3$ at 1.6 and 0.05 K collected at the D1B diffractometer. The closed circle (red) and the solid line (black) represent the experimental and calculated intensities, respectively, and the line below (blue) is the difference between them. Tick marks (green) indicate the position of Bragg peaks in the $R\bar{3}c$ space group. The large peak at around 75 ° is the nuclear Bragg peak of Cu from the sample holder, for which the calculated intensity is shown by the broken line. The down arrows show the magnetic Bragg peaks. (b) Rietveld refinement of the magnetic intensities obtained by subtracting the pattern at 1.6 K from that at 0.05 K. (c) The canted AFM structure of $NdPt_6Al_3$ in which the ordered moment of 2.62(2) $\mu_B$ lies in the honeycomb plane. The arrangement of magnetic moments in a hexagon is shown in the inset of (b).

CEF parameters, the magnetization components of $\mu_x$ and $\mu_z$ at 1.8 K and in an applied field of 8.5 T are calculated as 2.7 $\mu_B$ and 0.6 $\mu_B$, respectively. The values of $\mu_x$ and $\mu_z$ are nearly equal to the observed ones of 2.8 $\mu_B$ and 0.8 $\mu_B$ for $M(B \parallel a)$ and $M(B \parallel c)$ at 8.5 T, respectively.

### E. Neutron powder diffraction

The neutron powder-diffraction data were analyzed to determine the canted AFM structure of $NdPt_6Al_3$ below $T_m = 1.2$ K. Figure 11(a) displays the diffraction patterns at 1.6 K $> T_m$ and 0.05 K $< T_m$ with a neutron wavelength of 2.524 Å. The refinement of the crystal structure at 1.6 K yielded the trigonal lattice parameters $a = 7.5141(6)$ Å and $c = 39.091(3)$ Å. Note that the peak marked by the arrows in the pattern at 0.05 K are significantly enhanced compared with those at 1.6 K. Figure 11(b) represents the differential intensity obtained by subtracting the intensity at 1.6 K from that at 0.05 K. It is noteworthy that all the peaks can be indexed with a propagation vector $\mathbf{k} = [0, 0, 0]$.

Magnetic symmetry analysis using the program BASIREPS [49,50] for Wyckoff site 12*c* of the Nd atoms with the centrosymmetric space group $R\bar{3}c$ returned six allowed irreducible representations (IRs). The basis vectors (BVs) of these IRs are given in Table SI of Supplemental Material [51]. Two of them ($\Gamma_5$ and $\Gamma_6$) have four basis vectors along the *a* and *b* axes of the honeycomb plane, while the rest four ($\Gamma_1$, $\Gamma_2$, $\Gamma_3$, and $\Gamma_4$) have each only one BV along the *c* axis. Out of the above six IRs, $\Gamma_5$ with BVs within the honeycomb plane gives the best refinement of the magnetic diffraction pattern, producing a ferromagnetic coupling to explain the small spontaneous moment in the honeycomb plane (for more detail, see Supplemental Material [51]). Since a neutron powder diffraction cannot determine the direction of magnetic moments in a trigonal system within the *a*-*b* basal plane, we assumed that the ferromagnetic component of $NdPt_6Al_3$ is pointing along the *a* axis.

The refinement of the difference between the data at 0.05 and 1.6 K is displayed in Fig. 11(b). The proposed magnetic structure of $NdPt_6Al_3$ is depicted in Fig. 11(c), whose magnetic space group is No. 15.85 *C*2/*c*.1 [52]. The ordered moment of the $Nd^{3+}$ ion was refined as 2.62(2) $\mu_B$, which is close to to 2.7 $\mu_B$ calculated for $\mu_x$ using the CEF model. As shown in the inset of Fig. 11(b), the NN $Nd^{3+}$ moments are canted from antiparallel alignment by an angle of 15 °.

Let us discuss what mechanism stabilizes the canted AFM structure in $NdPt_6Al_3$. One is the magnetic frustration in the honeycomb lattice [1,2,5,53]. Here, we summarize three important observations: (i) the frustration parameter $f \cong 3$, (ii) the full release of magnetic entropy $R\ln 2$ at $T_m$, and (iii) the size of the ordered magnetic moments in agreement with the CEF calculation for the $Nd^{3+}$ ion. These observations suggest that magnetic frustration is not strong enough to induce the canted AFM structure. The other mechanism is the DM interaction between the NN $Nd^{3+}$ moments. In the theoretical models of the perfect honeycomb lattice with threefold rotational symmetry, the DM interaction between not the NN bond but the NNN one is generally taken into account because the midpoint of the NNN bond is not an inversion center [21,54]. However, the *RE* hexagon in $REPt_6Al_3$ is centered by the Pt triangle as shown in Fig. 1(b). This local geometrical condition breaks the inversion symmetry at the midpoint of the NN *RE* bond, which activates the DM interaction between the

NN moments to cant each other. This mechanism proposed in previous works [36,37] has been verified by the determination of the magnetic structure of $NdPt_6Al_3$.

The present work on $NdPt_6Al_3$ provides insight into the CEF effect and the relation between the magnetic structure and DM interaction in the rare-earth based honeycomb intermetallic compounds $REPt_6Al_3$. One of the fundamental aspects is that the easy-plane anisotropy and the inelastic excitations can be explained by the trigonal CEF. This CEF model should be useful for understanding the magnetic anisotropy in isostructural compounds $REPt_6Al_3$ ($RE$ = Ce, Pr, Sm, and Tb). Another important finding is that the DM interaction between the NN moments works even in a perfect honeycomb lattice to stabilize a noncollinear AFM structure. This finding would open up future works to explore unconventional magnetic structures in honeycomb-lattice compounds.

## IV. SUMMARY AND CONCLUSIONS

We investigated the magnetic properties of the Nd–honeycomb-lattice compound $NdPt_6Al_3$ with the centrosymmetric trigonal space group $R\bar{3}c$. Our magnetic-, transport-, and specific-heat measurements using single-crystalline samples revealed a long-range magnetic order at $T_m = 1.2$ K, where the Nd moments lie in the honeycomb plane. The small spontaneous moment of 0.2 $\mu_B$/f.u. in the honeycomb plane indicates the canted AFM order. The easy-plane magnetic anisotropy, the inelastic excitations (at 0.6 and 2.9 meV), and the Schottky anomalies (at 3 and 14 K) are explained on the basis of the CEF model of the trigonal point group $C_3$. The analysis of the neutron powder-diffraction data determined the canted AFM ordered state with the propagation vector $\mathbf{k} = [0, 0, 0]$, where the nearest-neighbor $Nd^{3+}$ moments cant from antiparallel alignment by the angle of 15°. We propose that the canting of the $Nd^{3+}$ moments results from the DM interaction between the nearest-neighbor $Nd^{3+}$ moments in the honeycomb structure with the centrosymmetric space group $R\bar{3}c$.

## ACKNOWLEDGMENTS

We thank D. Khalyavin and L. Pascut for valuable discussions. This work was supported by JSPS KAKENHI Grants No. JP21K03473, No. JP22J20278, No. JP22KJ2336, No. JP22K03529, and No. JP23H04870, and JST FOREST Grant No. JPMJFR2233. The low-temperature measurements and electron-probe microanalysis were performed at Integrated Experimental Support/Research Division, N-BARD, Hiroshima University. D.T.A. would like to thank the Royal Society of London for the International Exchange funding between the UK and Japan and EPSRC-UK for Grant No. EP/W00562X/1. D.T.A thanks the CAS for PIFI fellowship. We also thank ILL, for beam time on PANTHER (Exp No.4–04–512) [39] and D1B (Exp No.5–31–2957) [41].

[1] S. Katsura, T. Ide, and T. Morita, The ground states of the classical Heisenberg and planar models on the triangular and plane hexagonal lattices, J. Stat. Phys. **42**, 381 (1986).

[2] J. B. Fouet, P. Sindzingre, and C. Lhuillier, An investigation of the quantum $J_1$-$J_2$-$J_3$ model on the honeycomb lattice, Eur. Phys. J. B **20**, 241 (2001).

[3] P. H. Y. Li, R. F. Bishop, D. J. J. Farnell, and C. E. Campbell, Phase diagram of a frustrated Heisenberg antiferromagnet on the honeycomb lattice: The $J_1$-$J_2$-$J_3$ model, Phys. Rev. B **86**, 144404 (2012).

[4] P. F. Dias and M. Schmidt, Zigzag phase transition in the frustrated Ising honeycomb lattice, Phys. Rev. B **108**, 014436 (2023).

[5] J. Reuther, R. Thomale, and S. Rachel, Spiral order in the honeycomb iridate $Li_2IrO_3$, Phys. Rev. B **90**, 100405(R) (2014).

[6] S.-S. Gong, W. Zhu, and D. N. Sheng, Quantum phase diagram of the spin-1 $J_1$-$J_2$ Heisenberg model on the honeycomb lattice, Phys. Rev. B **92**, 195110 (2015).

[7] P. H. Y. Li and R. F. Bishop, Ground-state phases of the spin-1 $J_1$-$J_2$ Heisenberg antiferromagnet on the honeycomb lattice, Phys. Rev. B **93**, 214438 (2016).

[8] A. F. Albuquerque, D. Schwandt, B. Hetényi, S. Capponi, M. Mambrini, and A. M. Läuchli, Phase diagram of a frustrated quantum antiferromagnet on the honeycomb lattice: Magnetic order versus valence-bond crystal formation, Phys. Rev. B **84**, 024406 (2011).

[9] F. Ferrari and F. Becca, Dynamical properties of Néel and valence-bond phases in the $J_1$-$J_2$ model on the honeycomb lattice, J. Phys.: Condens. Matter **32**, 274003 (2020).

[10] *Frustrated Spin Systems*, 2nd ed., edited by H. Diep (World Scientific, Singapore, 2013).

[11] E. A. Zvereva, M. I. Stratan, Y. A. Ovchenkov, V. B. Nalbandyan, J.-Y. Lin, E. L. Vavilova, M. F. Iakovleva, M. Abdel-Hafiez, A. V. Silhanek, X.-J. Chen, A. Stroppa, S. Picozzi, H. O. Jeschke, R. Valentí, and A. N. Vasiliev, Zigzag antiferromagnetic quantum ground state in monoclinic honeycomb lattice antimonates $A_3Ni_2SbO_6$ ($A$ = Li, Na), Phys. Rev. B **92**, 144401 (2015).

[12] P. Yadav, S. Lee, G. L. Pascut, J. Kim, M. J. Gutmann, X. Xu, B. Gao, S.-W. Cheong, V. Kiryukhin, and S. Choi, Noncollinear magnetic order, in-plane anisotropy, and magnetoelectric coupling in the pyroelectric honeycomb antiferromagnet $Ni_2Mo_3O_8$, Phys. Rev. Res. **5**, 033099 (2023).

[13] A. Liu, F. Song, H. Bu, Z. Li, M. Ashtar, Y. Qin, D. Liu, Z. Xia, J. Li, Z. Zhang, W. Tong, H. Guo, and Z. Tian, $Ba_9RE_2(SiO_4)_6$ ($RE$ = Ho-Yb): A family of rare-earth-based honeycomb-lattice magnets, Inorg. Chem **62**, 13867 (2023).

[14] A. Kitaev, Anyons in an exactly solved model and beyond, Ann. Phys. **321**, 2 (2006).

[15] S. Trebst and C. Hickey, Kitaev materials, Phys. Rep. **950**, 1 (2022).

[16] S. Hayami, H. Kusunose, and Y. Motome, Toroidal order in metals without local inversion symmetry, Phys. Rev. B **90**, 024432 (2014).

[17] S. Hayami, H. Kusunose, and Y. Motome, Asymmetric magnon excitation by spontaneous toroidal ordering, J. Phys. Soc. Jpn. **85**, 053705 (2016).

[18] I. Dzyaloshinsky, A thermodynamic theory of "weak" ferromagnetism of antiferromagnetics, J. Phys. Chem. Solids **4**, 241 (1958).

[19] T. Moriya, Anisotropic superexchange interaction and weak ferromagnetism, Phys. Rev. **120**, 91 (1960).

[20] S. K. Kim, H. Ochoa, R. Zarzuela, and Y. Tserkovnyak, Realization of the Haldane-Kane-Mele model in a system of localized spins, Phys. Rev. Lett. **117**, 227201 (2016).

[21] S. A. Owerre, A first theoretical realization of honeycomb topological magnon insulator, J. Phys.: Condens. Matter **28**, 386001 (2016).

[22] M. Frontzek, A. Kreyssig, M. Doerr, A. Schneidewind, J.-U. Hoffmann, and M. Loewenhaupt, Frustration in $R_2PdSi_3$ ($R$ = Tb, Er) compounds: Spin-glass or magnetic short range order? Neutron diffraction studies, J. Phys.: Condens. Matter **19**, 145276 (2007).

[23] M. Cong, H. Ge, L. Zhang, W. Ren, N. Zhao, T. Li, S. Wang, J. Zhu, J. Mei, Q. Zhang, J. Sheng, F. Gao, B. Li, Z. Zhang, and L. Wu, Magnetic phase diagram and multiple field-induced states in the intermetallic triangular-lattice antiferromagnet $NdAuAl_4Ge_2$ with Ising-like spins, Phys. Rev. Mater. **7**, 024423 (2023).

[24] F. Gao, W. Ren, C.-W. Wang, S. Yano, S. Calder, Q. Zhang, H. Wu, M. An, Y. Jing, B. Li, and Z. Zhang, High-order harmonics and the reverse of the squaring up process in the triangular-lattice magnet $HoPdAl_4Ge_2$, Phys. Rev. B **109**, 134407 (2024).

[25] V. M. T. Thiede, B. Fehrmann, and W. Jeitschko, Ternary rare earth metal palladium and platinum aluminides $R_4Pd_9Al_{24}$ and $R_4Pt_9Al_{24}$, Z. Anorg. Allg. Chem. **625**, 1417 (1999).

[26] J. Niermann, B. Fehrmann, M. W. Wolff, and W. Jeitschko, Preparation and crystal structure of ternary rare-earth platinum metal aluminides $R_2T_3Al_9$ ($T$ = Rh, Ir, Pd) with $Y_2Co_3Ga_9$-type structure and magnetic properties of the iridium compounds, J. Solid State Chem. **177**, 2600 (2004).

[27] O. Sichevych, Y. Prots, Y. Utsumi, L. Akselrud, M. Schmidt, U. Burkhardt, M. Coduri, W. Schenelle, M. Bobnar, Y.-T. Wang, Y.-H. Wu, K.-D. Tsuei, L. H. Tjeng, and Y. Grin, Intermediate-valence ytterbium compound $Yb_4Ga_{24}Pt_9$: Synthesis, crystal structure, and physical properties, Inorg. Chem. **56**, 9343 (2017).

[28] M. Radzieowski, F. Stegemann, and O. Janka, Magnetic properties of the $RE_2Pt_6X_{15}$ ($RE$ = Y, La-Nd, Sm, Gd-Lu; $X$ = Al, Ga) series, Eur. J. Inorg. Chem. **2020**, 1199 (2020).

[29] R. E. Gladyshevskii, K. Cenzual, H. D. Flack, and E. Parthé, Structure of $RNi_3Al_9$ ($R$ = Y, Gd, Dy, Er) with either ordered or partly disordered arrangement of al-atom triangles and rare-earth-metal atoms, Acta Crystallogr. B **49**, 468 (1993).

[30] P. H. Tobash, Y. Jiang, F. Ronning, C. H. Booth, J. D. Thompson, B. L. Scott, and E. D. Bauer, Synthesis, structure and physical properties of $YbNi_3Al_{9.23}$, J. Phys.: Condens. Matter **23**, 086002 (2011).

[31] F. Eustermann, F. Stegemann, K. Renner, and O. Janka, Platinum triangles in the Pt/Al framework of the intermetallic $REPt_6Al_3$ ($RE$ = Ce-Nd, Sm, Gd, Tb) Series, Z. Anorg. Allg. Chem. **643**, 1836 (2017).

[32] T. Matsumura, Y. Kita, K. Kubo, Y. Yoshikawa, S. Michimura, T. Inami, Y. Kousaka, K. Inoue, and S. Ohara, Chiral soliton lattice formation in monoaxial helimagnet $Yb(Ni_{1-x}Cu_x)_3Al_9$, J. Phys. Soc. Jpn. **86**, 124702 (2017).

[33] M. Tsukagoshi, T. Matsumura, S. Michimura, T. Inami, and S. Ohara, Competition between helimagnetic and ferroquadrupolar ordering in a monoaxial chiral magnet $DyNi_3Ga_9$ studied by resonant x-ray diffraction, Phys. Rev. B **105**, 014428 (2022).

[34] S. Nakamura, T. Matsumura, K. Ohashi, H. Suzuki, M. Tsukagoshi, K. Kurauchi, H. Nakao, and S. Ohara, Discovery of antiferromagnetic chiral helical ordered state in trigonal $GdNi_3Ga_9$, Phys. Rev. B **108**, 104422 (2023).

[35] L. S. Silva, S. G. Mercena, D. J. Garcia, E. M. Bittar, C. B. R. Jesus, P. G. Pagliuso, R. Lora-Serrano, C. T. Meneses, and J. G. S. Doque, Crystal field effects in the intermetallic $RNi_3Ga_9$ ($R$ = Tb, Dy, Ho, and Er) compounds, Phys. Rev. B **95**, 134434 (2017).

[36] R. Oishi, Y. Shimura, K. Umeo, T. Onimaru, and T. Takabatake, $GdPt_6Al_3$: A canted antiferromagnet with a honeycomb structure, J. Phys. Soc. Jpn. **91**, 124706 (2022).

[37] R. Oishi, Y. Shimura, K. Umeo, T. Onimaru, T. Matsumura, M. Tsukagoshi, K. Kurauchi, H. Nitta, and T. Takabatake, Collinear antiferromagnet $SmPt_6Al_3$ with a Sm honeycomb structure centered by Pt triangles, J. Phys. Soc. Jpn. **93**, 034707 (2024).

[38] B. Fåk, S. Rols, G. Manzin, and O. Meulien, Panther—the new thermal neutron time-of-flight spectrometer at the ILL, EPJ Web Conf. **272**, 02001 (2022).

[39] D. T. Adroja and M. M. Koza, Crystal field-excitations of a honeycomb lattice $CePt_6Al_3$ with Pd-doping and reference compound $NdPt_6Al_3$, doi:10.5291/ILL-DATA.4-04-512.

[40] O. Arnold *et al.*, Mantid-Data analysis and visualization package for neutron scattering and $\mu$SR experiments, Nucl. Instrum. Methods Phys. Res., Sect. A **764**, 156 (2014).

[41] D. T. Adroja, V. Nassif, and C. Ritter, Canted magnetic structure of a Honeycomb lattice $NdPt_6Al_3$ using neutron diffraction, doi:10.5291/ILL-DATA.5-31-2957.

[42] J. Rodrìguez-Carvajal, Recent advances in magnetic structure determination by neutron powder diffraction, Phys. B (Amsterdam, Neth.) **192**, 55 (1993).

[43] H. Cho, M. Kratochvílová, N. Lee, H. Sim, and J.-G. Park, Frustrated antiferromagnetic honeycomb-tunnel-like lattice $CuR_2Ge_2O_8$ ($R$ = Pr, Nd, Sm, and Eu), Phys. Rev. B **96**, 224427 (2017).

[44] R. Oishi, Y. Ohmagari, Y. Kusanosem, Y. Yamane, K. Umeo, Y. Shimura, T. Onimaru, and T. Takabatake, Heavy-fermion behavior in a honeycomb Kondo lattice $CePt_6Al_3$, J. Phys. Soc. Jpn. **89**, 104705 (2020).

[45] G. H. Kwei, A. C. Lawson, A. C. Larson, B. Morosin, E. M. Larson, and P. C. Canfield, Structure of $Ce_2Pt_6Ga_{15}$: Interplanar disorder from the $Ce_2Ga_3$ layers, Acta Crystallogr., Sect. B **52**, 580 (1996).

[46] C. Tabata, F. Kon, K. Ota, R. Hibino, Y. Matsumoto, H. Amitsuka, H. Nakao, Y. Haga, and K. Kaneko, Magnetic order in honeycomb layered $U_2Pt_6Ga_{15}$ studied by resonant x-ray and neutron scattering, Phys. Rev. B **109**, 134403 (2024).

[47] B. R. Cooper, Theory of the spin wave contribution to the specific heat of dysprosium, Proc. Phys. Soc. **80**, 1225 (1962).

[48] K. W. H. Stevens, Matrix elements and operator equivalents connected with the magnetic properties of rare earth ions, Proc. Phys. Soc., Sect. A **65**, 209 (1952).

[49] J. Rodríguez-Carvajal, BASIREPS: A program for calculating irreducible representations of space groups and basis functions for axial and polar vector properties, part of the FullProf Suite of programs, https://www.ill.eu/sites/fullprof/.

[50] C. Ritter, Neutrons not entitled to retire at the age of 60: More than ever needed to reveal magnetic structures, Solid State Phenom. **170**, 263 (2011).

[51] See Supplemental Material at http://link.aps.org/supplemental/10.1103/PhysRevB.110.144411 for symmetry analysis of magnetic structure of $NdPt_6Al_3$.

[52] J. M. Perez-Mato, S. V. Gallego, E. S. Tasci, L. Elcoro, G. de la Flor, and M. I. Aroyo, Symmetry-based computational tools for magnetic crystallography, Annu. Rev. Matter Res. **45**, 217 (2015).

[53] A. Biffin, R. D. Johnson, I. Kimchi, R. Morris, A. Bombardi, J. G. Analytis, A. Vishwanath, and R. Coldea, Noncoplanar and counterrotating incommensurate magnetic order stabilized by kitaev interactions in $\gamma$-$Li_2IrO_3$, Phys. Rev. Lett. **113**, 197201 (2014).

[54] K. H. Lee, S. B. Chung, K. Parkm, and J.-G. Park, Magnonic quantum spin Hall state in the zigzag and stripe phases of the antiferromagnetic honeycomb lattice, Phys. Rev. B **97**, 180401(R) (2018).